NASA/TP—2004-213112

Stereo Imaging Velocimetry Technique Using Standard Off-the-Shelf CCD Cameras

Mark McDowell
Glenn Research Center, Cleveland, Ohio

Elizabeth Gray
Scientific Consulting, Inc., Cleveland, Ohio

December 2004

The NASA STI Program Office . . . in Profile

Since its founding, NASA has been dedicated to the advancement of aeronautics and space science. The NASA Scientific and Technical Information (STI) Program Office plays a key part in helping NASA maintain this important role.

The NASA STI Program Office is operated by Langley Research Center, the Lead Center for NASA's scientific and technical information. The NASA STI Program Office provides access to the NASA STI Database, the largest collection of aeronautical and space science STI in the world. The Program Office is also NASA's institutional mechanism for disseminating the results of its research and development activities. These results are published by NASA in the NASA STI Report Series, which includes the following report types:

- TECHNICAL PUBLICATION. Reports of completed research or a major significant phase of research that present the results of NASA programs and include extensive data or theoretical analysis. Includes compilations of significant scientific and technical data and information deemed to be of continuing reference value. NASA's counterpart of peer-reviewed formal professional papers but has less stringent limitations on manuscript length and extent of graphic presentations.

- TECHNICAL MEMORANDUM. Scientific and technical findings that are preliminary or of specialized interest, e.g., quick release reports, working papers, and bibliographies that contain minimal annotation. Does not contain extensive analysis.

- CONTRACTOR REPORT. Scientific and technical findings by NASA-sponsored contractors and grantees.

- CONFERENCE PUBLICATION. Collected papers from scientific and technical conferences, symposia, seminars, or other meetings sponsored or cosponsored by NASA.

- SPECIAL PUBLICATION. Scientific, technical, or historical information from NASA programs, projects, and missions, often concerned with subjects having substantial public interest.

- TECHNICAL TRANSLATION. English-language translations of foreign scientific and technical material pertinent to NASA's mission.

Specialized services that complement the STI Program Office's diverse offerings include creating custom thesauri, building customized databases, organizing and publishing research results . . . even providing videos.

For more information about the NASA STI Program Office, see the following:

- Access the NASA STI Program Home Page at ***http://www.sti.nasa.gov***

- E-mail your question via the Internet to help@sti.nasa.gov

- Fax your question to the NASA Access Help Desk at 301–621–0134

- Telephone the NASA Access Help Desk at 301–621–0390

- Write to:
  NASA Access Help Desk
  NASA Center for AeroSpace Information
  7121 Standard Drive
  Hanover, MD 21076

NASA/TP—2004-213112

Stereo Imaging Velocimetry Technique Using Standard Off-the-Shelf CCD Cameras

Mark McDowell
Glenn Research Center, Cleveland, Ohio

Elizabeth Gray
Scientific Consulting, Inc., Cleveland, Ohio

National Aeronautics and
Space Administration

Glenn Research Center

December 2004

Available from

NASA Center for Aerospace Information
7121 Standard Drive
Hanover, MD 21076

National Technical Information Service
5285 Port Royal Road
Springfield, VA 22100

Available electronically at http://gltrs.grc.nasa.gov

Stereo Imaging Velocimetry Technique Using Standard Off-the-Shelf CCD Cameras

Mark McDowell
National Aeronautics and Space Administration
Glenn Research Center
Cleveland, Ohio 44135

Elizabeth Gray
Scientific Consulting, Inc.
Cleveland, Ohio 44135

Summary

Stereo imaging velocimetry is a fluid physics technique for measuring three-dimensional (3D) velocities at a plurality of points. This technique provides full-field 3D analysis of any optically clear fluid or gas experiment seeded with tracer particles. Unlike current 3D particle imaging velocimetry systems that rely primarily on laser-based systems, stereo imaging velocimetry uses standard off-the-shelf charge-coupled device (CCD) cameras to provide accurate and reproducible 3D velocity profiles for experiments that require 3D analysis. Using two cameras aligned orthogonally, we present a closed mathematical solution resulting in an accurate 3D approximation of the observation volume. The stereo imaging velocimetry technique is divided into four phases: 3D camera calibration, particle overlap decomposition, particle tracking, and stereo matching. Each phase is explained in detail. In addition to being utilized for space shuttle experiments, stereo imaging velocimetry has been applied to the fields of fluid physics, bioscience, and colloidal microscopy.

Introduction

Stereo imaging velocimetry (SIV) is a new, affordable method for obtaining quantitative, three-dimensional (3D) flow information from any transparent liquid, gas, or air experiment seeded with tracer particles. Until recently, accurate flow information of this kind was very difficult to obtain and often required the use of sophisticated, dedicated laser-based measurement systems, which can lead to added safety concerns as well as increased costs. SIV provides a nonintrusive means for measuring 3D fluid velocities at many points and at high frame speeds by using charge-coupled device (CCD) video cameras and artificial neural-network-based computational algorithms. SIV, which was developed for NASA's microgravity science experiments as well as industrial applications, is the world's first 3D full-field quantitative and qualitative diagnostic tool (McDowell and Glasgow, 1999),

A typical SIV system consists of at least two CCD cameras, oriented 90° with respect to each other (orthogonal), observing an experiment that has been seeded with neutrally buoyant tracer particles that are imaged as the experiment is run. Each camera records two-dimensional (2D) data of the motion of the tracer particles in the observation volume, and 3D data are obtained by computationally combining the 2D information. Prior to running an experiment, the observation volume must be calibrated in order to generate a 2D to 3D mapping of the experiment. Once the experimental data are captured, the data are optimized by performing centroid determination with overlap decomposition, which increases the particle yield by separating overlapping particles into constituent particles. These data are used to perform particle tracking and stereo matching, resulting in the calculation of 3D velocity vectors. A description of each phase and examples follow. In addition, a symbols list is provided in the appendix.

Three-Dimensional Camera Calibration

Three-dimensional camera calibration is a process by which one determines the geometrical and experimental parameters for a particular experimental chamber and imaging system. The geometrical parameters are the internal camera characteristics, such as the focal length

and pixel size. The experimental parameters are the orientation of the cameras and chamber relative to a world coordinate system, the refractive characteristics of the system, and any lens aberrations or distortions present in the cameras. Camera calibration is the most important aspect of any machine vision experiment since it serves as a lower limit for determining system accuracy and permits us to make the jump from qualitative to quantitative data. The nomenclature of the SIV 3D camera calibration is shown in figure 1.

Following the steps outlined by Bethea et al. (1997) in analyzing the stereo imaging geometry shown in figure 1 and utilizing a known physical model and calculations using a theoretical model, one can determine the camera calibration error associated with a typical SIV experiment. In their experimental validation of a typical 3D camera calibration, Bethea et al. (1997), calculated the theoretical camera calibration accuracy to within 1.3 pixels and an experimental camera calibration to within 3.43 pixels. This indicates that the camera calibration

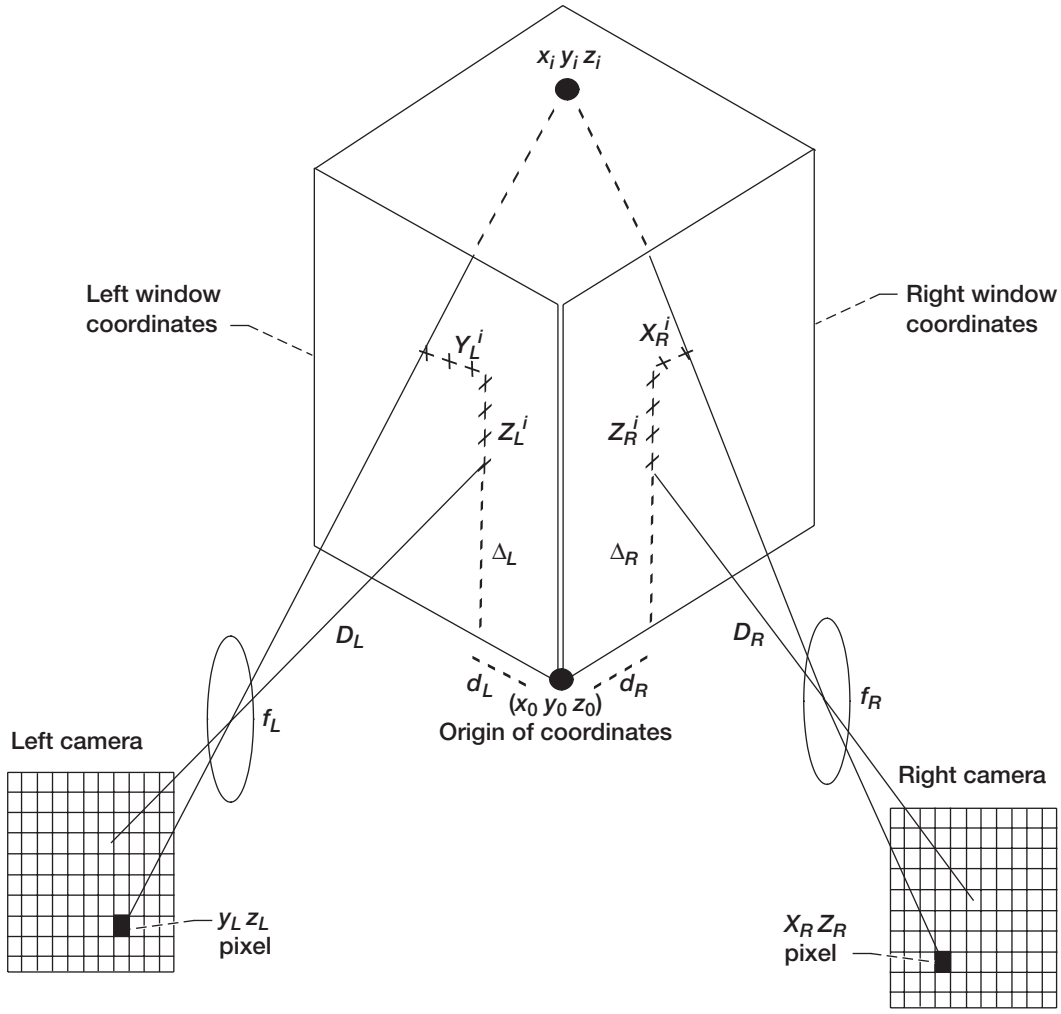

$x_i\ y_i\ z_i$	absolute *x y z* coordinates of particle *i*
$X_R^i Z_R^i$ ($Y_L^i\ Z_L^i$)	window coordinates of particle *i* on the right (left) face of the chamber
Δ	vertical distance of the camera axis from the origin
D	distance between the camera and the face of the chamber
d	horizontal distance of the camera axis from the origin
f	focal length of the camera
$x_R^i z_R^i$ ($y_L^i z_L^i$)	pixel coordinates of particle *i* as seen by the right (left) camera

Subscripts
L left camera
R right camera

Figure 1.—Camera calibration nomenclature, right camera perspective (left camera is analogous).

technique can accurately calibrate a 3D volume to within a typical particle size.

Calibration is performed using a target containing calibration points at known locations inserted into the experiment chamber and imaged by the right and left cameras. Two-dimensional calibrations are separately performed for the right and left cameras and then combined to form a 3D calibration. For each 2D calibration, it is possible to define an equation from the known absolute coordinates (x_i, y_i, z_i) to the pixel coordinates measured by the camera, with parameters including the rotation, magnification, pixel size, and aberration coefficients of the camera. The known absolute coordinates of the calibration points and the measured pixel locations are used as input to a least-squares data-fitting procedure to solve for the calibration coefficients, A_i, B_i, C_i, and D_i, listed in equations (1) and (2). Once the calibration procedure is complete, the absolute coordinates (x_j, y_j, z_j), of a seed particle entrained in the flow can be determined from its pixel positions (x_R, z_R) and (y_L, z_L) on the camera focal planes (see Bethea, 1996).

As explained in detail by Bethea et al. (1997), the right-camera calibration equations are as follows:

$$
\begin{aligned}
x \approx\ & A_0 + A_1 x_R - A_2 z_R + A_3 x_R y - A_4 z_R y - A_5 x_R |x_R| - A_6 x_R |z_R| + A_7 |x_R| z_R + A_8 |z_R| z_R - A_9 x_R \left(|x_R \| z_R|\right)^{1/2} \\
& + A_{10} z_R \left(|x_R \| z_R|\right)^{1/2} - A_{11} x_R |x_R| y - A_{12} x_R |z_R| y + A_{13} z_R |x_R| y + A_{14} z_R |z_R| y - A_{15} x_R \left(|x_R \| z_R|\right)^{1/2} y \\
& + A_{16} z_R \left(|x_R \| z_R|\right)^{1/2} y + A_{17} x_R^3 - A_{18} x_R^2 z_R + A_{19} x_R z_R^2 - A_{20} z_R^3 + A_{21} x_R^3 y - A_{22} x_R^2 z_R y + A_{23} x_R z_R^2 y - A_{24} z_R^3 y \\
& + \ldots \\
z \approx\ & B_0 + B_1 x_R + B_2 z_R + B_3 x_R y + B_4 z_R y - B_5 x_R |x_R| - B_6 x_R |z_R| - B_7 |x_R| z_R - B_8 |z_R| z_R - B_9 x_R \left(|x_R \| z_R|\right)^{1/2} \\
& - B_{10} z_R \left(|x_R \| z_R|\right)^{1/2} - B_{11} x_R |x_R| y - B_{12} x_R |z_R| y - B_{13} z_R |x_R| y - B_{14} z_R |z_R| y - B_{15} x_R \left(|x_R \| z_R|\right)^{1/2} y \\
& - B_{16} z_R \left(|x_R \| z_R|\right)^{1/2} y + B_{17} x_R^3 + B_{18} x_R^2 z_R + B_{19} x_R z_R^2 + B_{20} z_R^3 + B_{21} x_R^3 y + B_{22} x_R^2 z_R y + B_{23} x_R z_R^2 y + B_{24} z_R^3 y \\
& + \ldots
\end{aligned}
\tag{1}
$$

and the left-camera calibration equations are as follows:

$$
\begin{aligned}
y \approx\ & C_0 + C_1 y_L - C_2 y_L + C_3 y_L x - C_4 z_L x - C_5 y_L |y_L| - C_6 y_L |z_L| + C_7 |y_L| z_L + C_8 |z_L| z_L - C_9 y_L \left(|y_L \| z_L|\right)^{1/2} \\
& + C_{10} z_L \left(|y_L \| z_L|\right)^{1/2} - C_{11} y_L |y_L| x - C_{12} y_L |z_L| x + C_{13} z_L |y_L| x + C_{14} z_L |z_L| x - C_{15} y_L \left(|y_L \| z_L|\right)^{1/2} x \\
& + C_{16} z_L \left(|y_L \| z_L|\right)^{1/2} x + C_{17} y_L^3 - C_{18} y_L^2 z_L + C_{19} y_L z_L^2 - C_{20} z_L^3 + C_{21} y_L^3 x - C_{22} y_L^2 z_L x + C_{23} y_L z_L^2 x - C_{24} z_L^3 x \\
& + \ldots \\
z \approx\ & D_0 + D_1 y_L + D_2 z_L + D_3 y_L x + D_4 z_L x - D_5 y_L |y_L| - D_6 y_L |z_L| - D_7 |y_L| z_L - D_8 |z_L| z_L - D_9 y_L \left(|y_L \| z_L|\right)^{1/2} \\
& - D_{10} z_L \left(|y_L \| z_L|\right)^{1/2} - D_{11} y_L |y_L| x - D_{12} y_L |z_L| x - D_{13} z_L |y_L| x - D_{14} z_L |z_L| x - D_{15} y_L \left(|y_L \| z_L|\right)^{1/2} x \\
& - D_{16} z_L \left(|y_L \| z_L|\right)^{1/2} x + D_{17} y_L^3 + D_{18} y_L^2 z_L + D_{19} y_L z_L^2 + D_{20} z_L^3 + D_{21} y_L^3 x + D_{22} y_L^2 z_L x + D_{23} y_L z_L^2 x + D_{24} z_L^3 x \\
& + \ldots
\end{aligned}
\tag{2}
$$

where $A_0 = d_R$, $A_1 = (C_R D_R / f_R)\cos\varphi$, $A_2 = (C_R D_R / f_R)\sin\varphi$, $C_R =$ camera-dependent constant with units in millimeters per pixel, and so forth.

Particle Overlap Decomposition

After applying standard image preprocessing techniques, such as threshold, that separate objects from the background, we have images consisting of objects (i.e., particles) that need to be accurately identified. We first calculate the intensity-weighted center of mass of each object by using a technique described by Miller et al. (1994). Identification of the intensity-weighted center of mass of each object is important in establishing the true geometrical center of each object. The next step is to calculate and classify the plurality of each object, which we call overlap decomposition. Overlapping particles are a function of the degree to which the flow is seeded (data density or volume fraction of particles). They cause inaccurate centroid locations if the objects are not properly identified as consisting of more than one particle. This improper identification not only loses particles, but particle centroids are not accurate for any of the constituent particles. Hence, any miscalculations of centroid locations will result in a direct miscalculation of 2D velocities, at the least, and may lead to incorrect matches when stereo matching is performed, which will lead to large errors when 3D analysis is performed (see Guezennec and Kiritsis, 1990).

Our feature-based approach to overlap decomposition uses the major axis of the bounding ellipse and the circumference of the multiparticle object to determine the number of constituent particles and their respective locations. In general, the probability that the object region is composed of multiple overlapping particles increases as the circumference and major axis increase. This provides the basis for our overlapping particle algorithm. We have used many synthetic and real images to obtain the data required to empirically derive equations that describe these functional relationships. In our experiments, which were conducted in a constant volume with reasonable seeding densities on the order of 10 percent or less (higher densities begin to inhibit the flow), it is statistically improbable that an object region will be composed of more than three overlapping particles. Thus, the probability relationships between the major axis or circumference and the number of particles in the multiparticle objects were determined for up to three overlapping particles. In addition, both the major axis of the bounding ellipse and the circumference vary linearly with respect to the multiparticle object radius. This fact is significant because the probability relationships can be "learned" for one size of particle and be transposed to other experiments through function normalization (see Pao, 1989).

The major axis length requires an elliptical approximation of the object region. We accomplish this using the bounding ellipse algorithm presented by Haralick and Shapiro (1992). In addition to obtaining the major axis length, the algorithm finds the minor axis length and the orientation of the major axis with respect to the column axis of the CCD array. These data are essential to the decomposition of the object region into constituent centroid locations. The probability that an object region consists of a single, double, or triple particle can be obtained by following the extraction of the feature vector (major axis length, circumference). This is accomplished by entering the features into the empirically derived probability equations described in the following paragraphs and shown in figure 2. In all equations, x is the value of the feature.

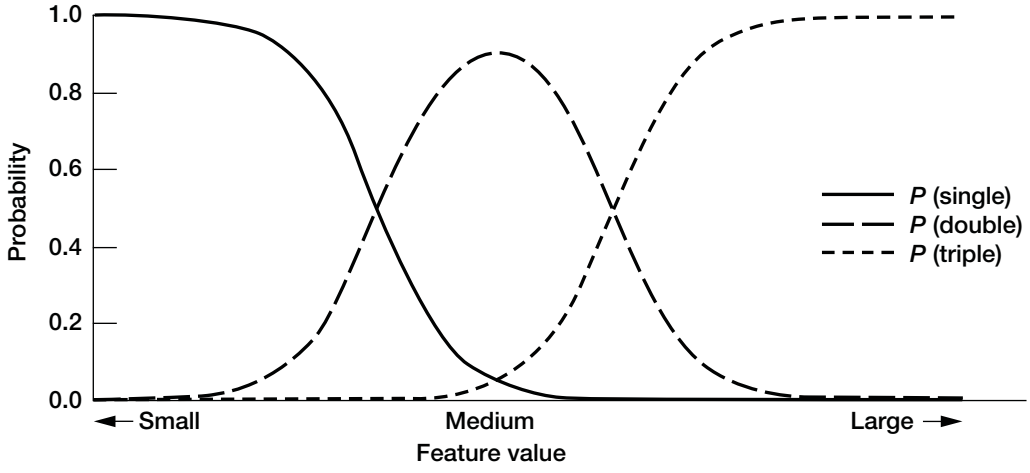

Figure 2.—Probability relationships for a single, double, and triple object.

The probabilities of a feature being a single, a double, or a triple particle are found for each feature independently, and then the results are combined. Because the circumference of the object is an exact measurement and the major axis is an approximation to the bounding ellipse, the circumference is given 50 percent more influence in the final classification.

The probability relationship equations have parameter values (q, b, t, and c) that must be defined in order to complete the algorithm. These parameters were determined by extensive training of an artificial neural network. They were optimized on the basis of the imaged size of particles from the training set (168-μm-diameter particles with an average imaged diameter of 2.1 pixels). We used the following values for q, b, t, and c:

Circumference

$q = -8.5$	$t = -0.16\,q$
$b = -16.5$	$c = -t$

Major axis

$q = 4.0$	$t = -0.14\,q$
$b = -7.3$	$c = -t$

The probability curves can be determined for any experimental training set, and once calculated, the maximum of the three probabilities can be used to determine the number of overlapping particles contained in the object. We can decompose into constituent centroid locations by using the centroid of the object, the major axis length, the minor axis length, the number of overlapping particles, and simple geometric relationships.

$$P(\text{single}) = 1 - \frac{1}{1 - e^{-\frac{x+q}{t}}}$$

$$P(\text{triple}) = 1 - \frac{1}{1 - e^{-\frac{x+b}{c}}}$$

$$P(\text{double}) = 1 - P(\text{single}) - P(\text{triple})$$

We tested our algorithm using synthetic data sets containing 50, 100, 150, and 180 particles (sample single images from data sets containing 100 and 180 particles are shown in figures 3 and 4) and on a random sample from a real data set containing approximately 200 particles (five consecutive sample images are shown in fig. 5). The results of the synthetic data experiment are given in table I, and the results for the real data are given in table II. The percentage of particles missed without using our overlap decomposition routine ranged from 4.4 to 12.1 percent, which can lead to significant particle identification errors.

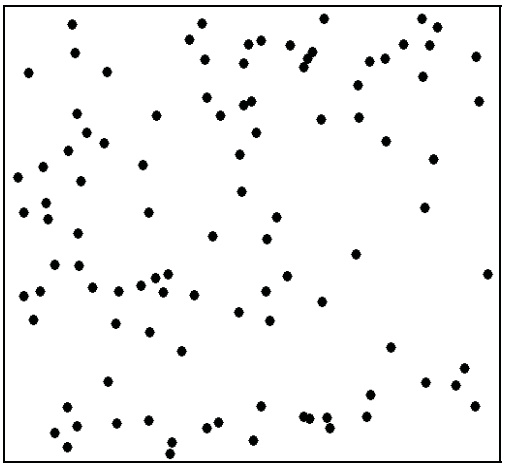

Figure 3.—Synthetic data sample image (100 particles).

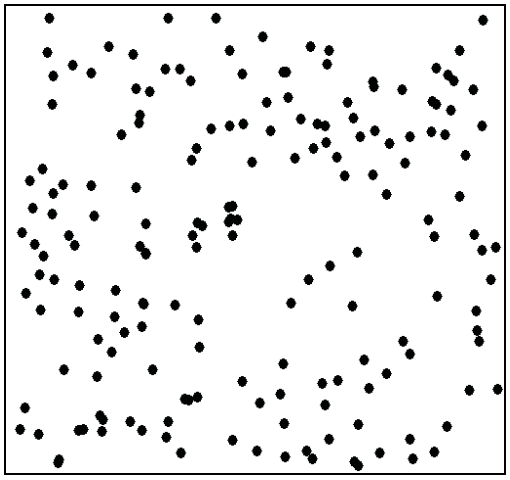

Figure 4.—Synthetic data sample image (180 particles).

It should be noted that the polystyrene particles used in this experiment do not bond well to each other and, therefore, have a relatively low adhesion property. Using particle materials with significant adhesion properties would effectively increase the detected particle sizes and negatively skew the results.

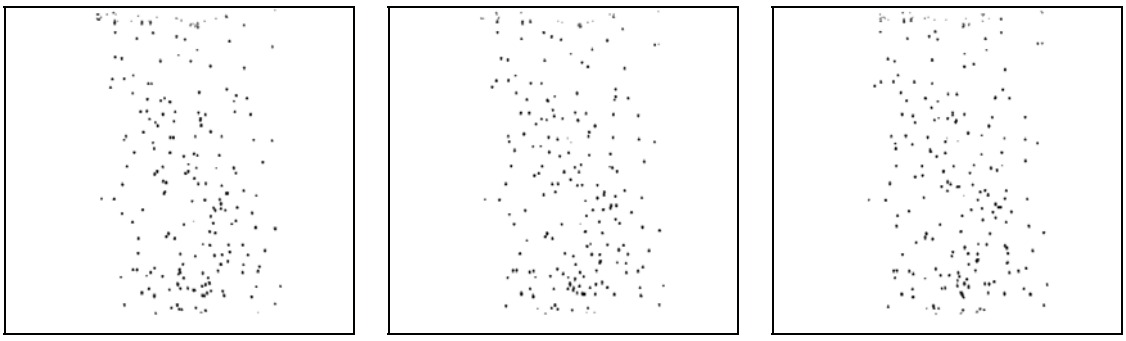

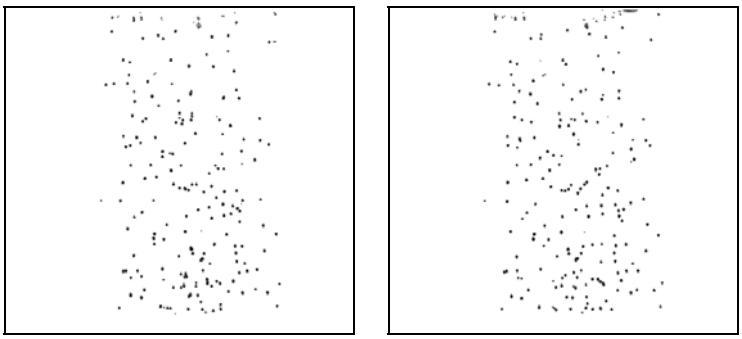

Figure 5.—Real image data from testbed experiment (five-frame sequence of approximately 200 particles).

TABLE I.—SYNTHETIC DATA PARTICLE YIELD
[Averaged over five images.]

Number of random particles	Average particle yield without overlap decomposition		Average particle yield with overlap decomposition			Data density, percent of full field
	Number of particles	Percent	Number of particles	Percent	Increase, percent	
50	47.6	95.2	49.8	99.6	4.4	1.6
100	93.0	93.0	99.6	99.6	6.6	3.3
150	134.0	89.3	148.8	99.2	9.9	4.9
180	156.4	86.9	178.2	99.0	12.1	5.7

TABLE II.—REAL DATA PARTICLE YIELD
[Averaged over five frames.]

Number of random particles	Yield with overlap decomposition		Data density, percent of full field
	Number of particles	Percent	
100	94.4	94.4	1.2
150	140.0	93.3	1.9
200	188.6	94.3	3.1
250	236.8	94.6	4.0
300	270.8	90.3	4.2

Particle Tracking

Particle tracking determines the motion of particles in either two or three dimensions by measuring the incremental distances moved by each particle between each frame. The success of a particle-tracking algorithm rests on several things: how heavily the flow is seeded, the frame rate of the image-acquisition hardware, and the velocity of the particles. If the flow is heavily seeded, it becomes more difficult to follow the motion of individual particles over time. The frame rate and particle velocity issues are intertwined; they relate to the problem of how many pixels a particle will move between consecutive frames. Although extremely slow velocities can be a problem because, eventually, the quantization errors inherent when using CCD cameras may make motion appear where none exists, this can be treated by slowing the frame rate so that significant motion takes place between frames. This technique is applicable when the flow is slow and uniform. High velocities present a more serious problem because current technology limits image acquisition and storage to 30 frames/sec for standard off-the-shelf cameras. The limitation this imposes on velocity depends on the configuration of the system, including the magnification and field of view. For example, the particle tracker can tolerate up to 30 particle diameters of motion between frames (if the field of view is at least this large). For particles spanning three pixels in diameter when imaged (the minimum recommended) and a frame rate of 30 frames/sec, this translates into a maximum velocity of 2700 pixels/sec. To translate this to a real-world value, we must take the magnification of the system into account. If the real-world size of a particle is 300 μm (0.03 cm) and its imaged size is 3 pixels, we have a scaling factor of 0.01 cm/pixel, giving a maximum velocity of 27 cm/sec.

Using information about the maximum expected velocity, we link particle identities through four frame sequences, establishing their paths of motion in the process. Our particle-tracking technique uses an adaptive, guided, evolutionary neural network with simulated annealing to arrive at a globally optimal assignment of tracks (see Crouser et al., 1995). The neural network is "guided" both by the minimization of the search space, through the use of limiting assumptions about valid tracks, and by a strategy that seeks to avoid high-energy intermediate states by eliminating overlapping tracks that can trap the neural network in a local minimum. A stochastic search algorithm is used to further reduce the chance of the neural network being trapped in an energy well. Global optimization is achieved by minimizing an objective function that includes both track smoothness and particle image utilization parameters.

Optimization begins by randomly choosing selections, called parents, from a database of complete sets of first guesses as to possible track assignments. These early parents are poor solutions and need to be optimized. We do this by randomly selecting one or more tracks within a parent, changing the track(s), and calling the resultant modified solution a child. Several children per parent are generated to create a family. Families evolve when a new generation of parents is chosen from among the existing family members. The system error (the objective function to be minimized) is computed for each child, and the member of a given family with the lowest system error becomes the new parent. The process is repeated over many generations until an acceptable solution is found or until the families stop evolving. The latter can occur because the best solution was found or because a local minimum in the system error or an energy well was found. Figure 6 describes how we determine a valid track pattern.

System error is a relative measure of the acceptability of a given state. Ideally, every particle in every frame should be assigned to a single track with the assumption that the particle overlap decomposition algorithm has correctly resolved overlapping particles into distinct objects. This is expressed in the system error by a "particle_usage error" term, which is multiplied by a scaling factor based on the particle size termed "usageCoeff."

Particle utilization by itself is not enough information to determine correct tracks. The only other information available is track straightness and track smoothness (fig. 7). Tracks are biased both by how straight they are (an assumption of zero acceleration when estimating the particle position in frame 3) and by how well the fourth particle in the track conforms to the position predicted for it by a pair of parametric quadratic equations in the x and y directions. These equations are derived from the preceding three particles in that track. The former error is referred to as the "track straightness error," whereas the latter error is referred to as the "track smoothness error."

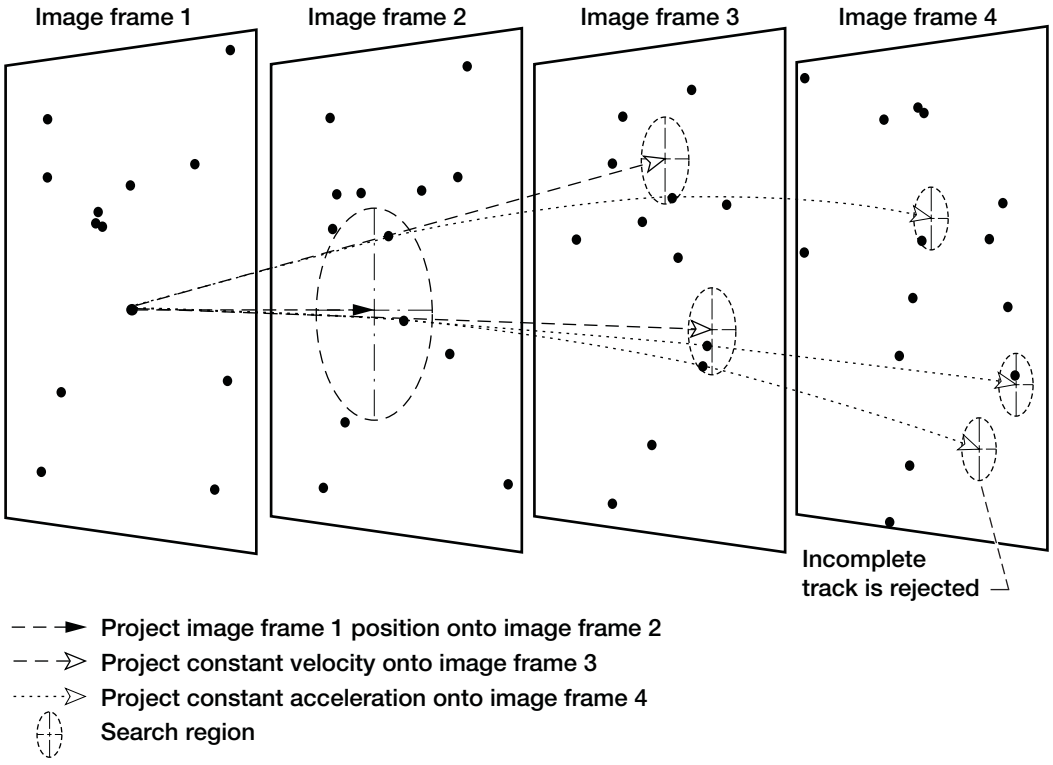

Figure 6.—Schematic of how potentially valid tracks are identified. An empty search region terminates a track fragment. In this example, two valid tracks are identified for the original particle. The process is continued until only the valid track remains or until an energy well is encountered.

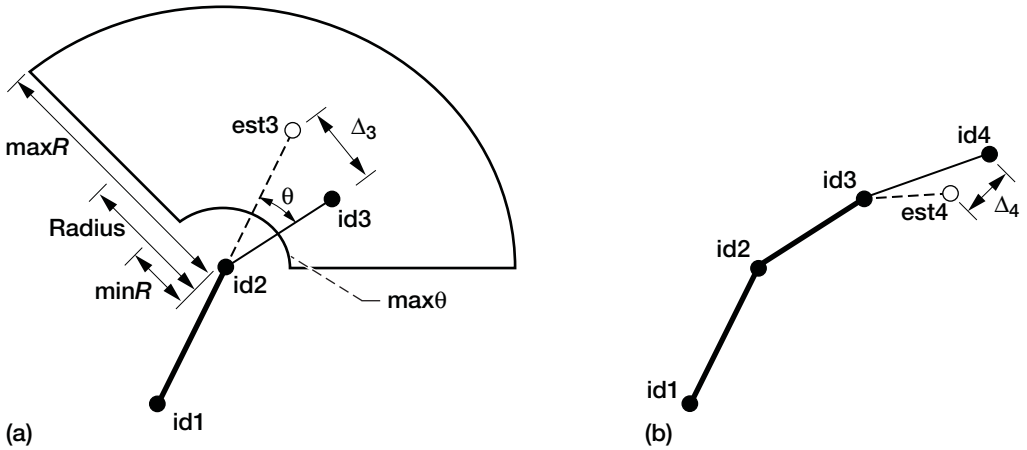

Figure 7.—Track errors, where Δ_3 measures the difference between the actual and estimated position (based on an assumption of zero acceleration) of a particle in frame 3, Δ_4 measures the difference between the actual and estimated position (based on an assumption of constant acceleration) of a particle in frame 4, est is the estimated position of a particle, id is the track identification number, and max*R* and min*R* are the maximum and minimum radii. (a) Track straightness error. (b) Track smoothness error.

Thus, the equation for system error becomes

$$\text{system\_error} = \text{track\_error} + \text{usageCoeff}\ (\text{particle\_usage\_error})$$

where

track_error	$\sum_{j=1}^{N_1} f$ (track_straightness_error[j], track_smoothness_error[j]
N_1	number of tracks (i.e., the number of particles in frame 1)
f ()	penalty function defined as a mapping from the parameters shown, with $-2.0 < f(\ ) < 2.0$ (see fig. 7)
usageCoeff	weighting of the usage error relative to the track error
particle_usage_error	$\sum_{f=1}^{F}\sum_{j=1}^{N_f}$ | assigned_particle_usage[f, j] – 1 |
F	number of frames in a track
N_f	number of particles in a frame f, $1 \le f \le F = 4$
assigned_particle_usage[f, j]	the number of times particle j in frame f appears within any track from a particular assignment of tracks

Figure 8 shows examples of typical left and right experiments of a 3D experiment image before particle tracking. Following preprocessing, the centroid-determination/overlap-decomposition algorithm was applied to these images to find the particles, decompose them, and determine their centroids. Tables III and IV give the overlap decomposition analysis of the left and right images. The data files resulting from the overlap

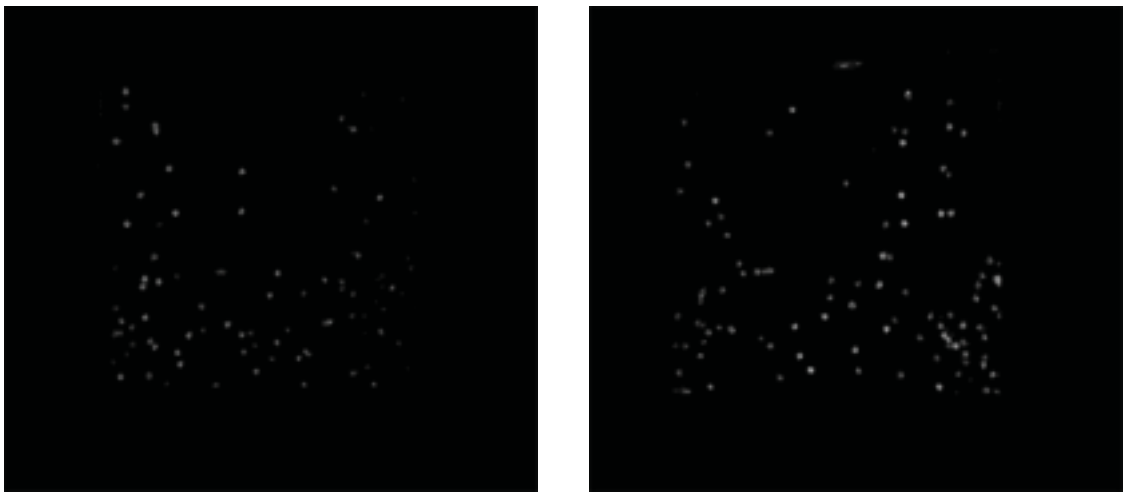

Figure 8.—Typical left and right image files.

TABLE III.—OVERLAP DECOMPOSITION ANALYSIS OF THE LEFT IMAGE DATA FILE

Coordinates		Number of particles in object			Order
x	y	Single	Double	Triple	
164.97	91.69	0.910	0.090	0.000	1
192.41	147.57	.934	.066	.000	1
237.75	183.56	.910	.090	.000	1
224.67	185.63	.910	.090	.000	1
276.90	187.72	.910	.090	.000	1
368.53	191.83	.934	.066	.000	1
366.69	201.89	.910	.090	.000	1
234.03	207.42	.910	.090	.000	1
285.64	208.40	.972	.028	.000	1
300.52	226.58	.955	.045	.000	1
256.85	240.74	.949	.050	.000	1
303.30	242.84	.702	.296	.001	1
338.34	242.06	.846	.153	.001	1
396.19	256.70	.972	.028	.000	1
228.32	261.92	.859	.140	.000	1
310.56	263.29	.910	.090	.000	1
323.61	263.42	.866	.134	.000	1
290.96	265.37	.910	.090	.000	1
374.34	285.73	.812	.188	.001	1
315.72	289.53	.866	.134	.000	1
328.76	289.59	.910	.090	.000	1
197.10	294.88	.206	.782	.012	2
196.46	292.45	.206	.782	.012	2
362.61	295.46	.812	.188	.001	1
274.27	302.57	.938	.062	.000	1
237.07	303.50	.910	.090	.000	1
277.61	302.50	.992	.008	.000	1
385.22	309.43	.910	.090	.000	1
274.89	316.52	.955	.045	.000	1
335.26	319.46	.910	.090	.000	1
323.75	320.96	.863	.137	.000	1
220.31	333.14	.846	.153	.001	1
357.71	333.65	.866	.134	.000	1
316.59	340.01	.896	.104	.000	1
337.28	342.30	.972	.028	.000	1
363.38	342.91	.896	.104	.000	1
243.38	344.73	.776	.223	.001	1
273.04	345.72	.799	.200	.001	1
194.97	345.57	.866	.134	.000	1
314.72	346.03	.846	.153	.001	1
236.01	347.35	.910	.090	.000	1
390.08	348.72	.969	.031	.000	1
313.93	353.71	.054	.735	.212	2
311.35	354.86	.054	.735	.212	2

Coordinates		Number of particles in object			Order
x	y	Single	Double	Triple	
285.24	353.53	0.866	0.134	0.000	1
194.54	355.15	.896	.104	.000	1
251.25	358.12	.028	.805	.167	2
249.02	360.25	.028	.805	.167	2
294.33	357.19	.896	.104	.000	1
176.82	359.42	.910	.090	.000	1
258.06	368.31	.960	.040	.000	1
310.15	373.70	.910	.090	.000	1
237.70	374.45	.955	.045	.000	1
204.24	385.53	.866	.134	.000	1
229.13	385.69	.910	.090	.000	1
240.49	388.38	.776	.223	.001	1
206.22	393.50	.866	.134	.000	1
258.48	393.59	.826	.174	.001	1
231.57	397.92	.896	.104	.000	1
222.02	406.81	.514	.483	.003	1
185.11	407.48	.896	.104	.000	1
268.13	410.65	.872	.128	.000	1
401.22	414.06	.938	.062	.000	1
243.47	416.60	.644	.354	.002	1
275.14	418.38	.107	.856	.037	2
273.86	420.71	.107	.856	.037	2
355.29	420.14	.896	.104	.000	1
235.92	421.34	.812	.188	.001	1
223.79	423.58	.803	.196	.001	1
284.54	425.42	.812	.188	.001	1
260.37	427.63	.866	.134	.000	1
317.67	428.37	.776	.223	.001	1
295.02	433.49	.910	.090	.000	1
258.42	439.27	.000	.085	.914	3
257.80	435.90	.000	.085	.914	3
259.04	442.64	.000	.085	.914	3
268.08	435.09	.812	.188	.001	1
246.28	442.76	.580	.418	.002	1
325.07	444.43	.324	.670	.006	2
327.49	444.36	.324	.670	.006	2
336.51	443.54	.826	.174	.001	1
291.73	445.34	.846	.153	.001	1
162.78	445.77	.869	.130	.000	1
269.22	448.99	.260	.731	.008	2
271.52	447.63	.260	.731	.008	2
319.74	447.69	.869	.130	.000	1
375.61	452.50	.992	.008	.000	1

TABLE IV.—OVERLAP DECOMPOSITION ANALYSIS OF THE RIGHT IMAGE DATA FILE

Coordinates		Number of particles in object			Order
x	*y*	Single	Double	Triple	
309.62	93.72	0.866	0.134	0.000	1
260.62	149.21	.910	.090	.000	1
170.87	185.54	.910	.090	.000	1
281.01	186.13	.938	.062	.000	1
313.40	187.38	.202	.787	.011	2
312.41	189.91	.202	.787	.011	2
348.76	200.58	.910	.090	.000	1
226.20	207.92	.866	.134	.000	1
375.50	207.02	.910	.090	.000	1
241.09	226.70	.972	.028	.000	1
187.11	241.34	.866	.134	.000	1
381.56	241.76	.618	.380	.002	1
225.35	242.57	.934	.065	.000	1
310.55	256.68	.955	.045	.000	1
281.91	261.80	.812	.188	.001	1
221.54	263.46	.826	.174	.001	1
302.24	263.41	.812	.188	.001	1
230.42	265.39	.866	.134	.000	1
235.58	285.44	.465	.531	.003	2
235.00	287.53	.465	.531	.003	2
128.89	289.61	.755	.244	.001	1
160.82	290.02	.812	.188	.001	1
262.73	290.85	.896	.104	.000	1
279.58	295.11	.689	.309	.002	1
156.23	295.77	.727	.272	.001	1
222.19	302.38	.955	.045	.000	1
229.62	303.16	.859	.140	.000	1
273.94	310.36	.929	.071	.000	1
294.65	319.68	.039	.843	.118	2
293.47	316.93	.039	.843	.118	2
187.21	320.48	.896	.104	.000	1
193.87	331.29	.866	.134	.000	1
169.11	333.86	.812	.188	.001	1
369.29	341.69	.866	.134	.000	1
219.65	343.43	.015	.830	.155	2
217.10	345.74	.015	.830	.155	2
202.97	343.14	.812	.188	.001	1
293.29	343.70	.812	.188	.001	1
317.61	343.37	.866	.134	.000	1
274.93	345.83	.869	.130	.000	1
314.04	350.45	.938	.062	.000	1
236.72	352.47	.929	.071	.000	1
251.12	352.99	.812	.188	.001	1
320.00	353.53	.869	.130	.000	1

Coordinates		Number of particles in object			Order
x	*y*	Single	Double	Triple	
260.51	355.39	0.812	0.188	0.001	1
202.80	355.85	.866	.134	.000	1
277.21	355.72	.866	.134	.000	1
360.85	357.89	.812	.188	.001	1
218.16	359.38	.654	.345	.002	1
301.61	367.74	.910	.090	.000	1
249.66	372.91	.896	.104	.000	1
268.50	373.74	.799	.200	.001	1
273.89	384.23	.859	.140	.000	1
302.58	383.64	.812	.188	.001	1
308.34	387.55	.664	.334	.002	1
301.58	391.24	.846	.153	.001	1
268.91	392.50	.776	.223	.001	1
249.38	395.70	.866	.134	.000	1
208.18	403.38	.581	.416	.003	1
271.09	403.65	.846	.153	.001	1
255.41	409.38	.812	.188	.001	1
194.44	413.40	.776	.223	.001	1
313.56	416.55	.955	.045	.000	1
164.69	417.74	.826	.174	.001	1
218.46	417.75	.689	.309	.002	1
399.60	419.65	.934	.066	.000	1
213.15	420.41	.896	.104	.000	1
351.72	422.37	.801	.199	.001	1
299.39	424.82	.896	.104	.000	1
310.67	426.55	.934	.065	.000	1
269.73	431.54	.068	.895	.037	2
272.36	429.97	.068	.895	.037	2
213.85	432.04	.748	.251	.001	1
246.40	433.31	.754	.245	.001	1
282.05	437.87	.689	.309	.002	1
202.33	439.35	.859	.140	.000	1
262.18	439.86	.812	.188	.001	1
168.94	441.74	.718	.281	.001	1
321.68	441.88	.718	.281	.001	1
160.87	442.49	.580	.418	.002	1
227.18	443.79	.689	.309	.002	1
235.35	447.46	.776	.223	.001	1
376.53	449.45	.524	.472	.004	1
205.16	451.09	.514	.483	.003	1
170.74	452.35	.929	.071	.000	1
227.44	452.50	.992	.008	.000	1
261.73	452.50	.981	.019	.000	1

decomposition were used as input to the tracking algorithm. Tables V and VI give the particle tracking results for the left and right images.

Stereo Matching

Stereo matching determines which of the many particle tracks in a pair of synched images from the two cameras represent the same particle track photographed from different perspectives. Given two sets of 2D tracks, one set from each of two orthogonal views, the stereo-matching module provides the ability to stereo match the tracks and determine a globally optimal solution (fig. 9). This module uses an evolutionary neural network model. Optimization error is taken to be the sum of the squared vertical displacements (in pixels) between corresponding particle images, on a frame-by-frame basis, matching

TABLE V.—TWO-DIMENSIONAL TRACKING RESULTS FOR THE LEFT IMAGE DATA FILE

Sequential index	Tracking index (four-frame sequence)			
0	0	0	0	0
1	1	1	1	1
2	2	3	4	4
3	3	2	2	2
4	4	4	3	3
5	5	5	5	5
6	6	6	6	6
7	7	7	7	8
8	8	8	8	7
9	9	9	9	9
10	10	10	11	12
11	11	11	10	10
12	12	12	12	11
13	13	13	13	15
14	14	14	14	13
15	15	15	17	17
16	16	16	15	14
17	17	17	16	16
18	18	18	18	18
19	19	19	19	20
20	20	22	22	24
21	21	21	20	19
22	22	20	21	21
23	23	23	23	22
24	24	24	24	23
25	25	25	25	25
26	26	–99	–99	–99
27	27	26	26	26
28	28	27	27	27
29	29	29	28	28
30	30	28	29	29
31	31	30	30	30
32	32	31	31	35
33	33	32	33	36
34	34	33	35	32
35	35	39	38	41
36	36	34	32	33
37	37	38	36	37
38	38	36	37	38
39	39	35	34	31
40	40	37	32	34
41	41	40	41	42
42	42	42	40	40
43	43	41	39	39
44	44	43	43	44
45	45	45	45	47
46	46	44	42	43
47	47	48	47	49
48	48	46	44	45
49	49	47	46	46
50	50	49	48	48
51	51	51	49	51
52	52	50	50	50
53	53	53	51	52
54	54	54	52	54
55	55	55	52	53
56	56	56	53	55
57	57	57	54	56
58	58	58	55	57
59	59	60	57	59
60	60	59	56	58
61	61	61	58	60
62	62	63	59	61
63	63	64	60	63
64	64	62	61	63
65	65	66	62	64
66	66	67	63	65
67	67	68	66	68
68	68	69	64	66
69	69	65	67	62
70	70	70	65	67
71	71	71	68	69
72	72	73	71	70
73	73	74	70	72
74	74	75	72	73
75	75	77	73	77
76	76	72	69	71
77	77	77	74	77
78	78	80	78	80
79	79	80	78	80
80	80	78	76	76
81	81	79	75	75
82	82	81	79	81
83	83	82	77	78
84	84	83	77	78
85	85	84	80	79
86	86	–99	–99	–99

TABLE VI.— TWO-DIMENSIONAL TRACKING RESULTS FOR THE RIGHT IMAGE DATA FILE

Sequential index	Tracking index (four-frame sequence)			
0	0	0	0	0
1	1	1	1	1
2	2	4	4	4
3	3	2	2	2
4	4	3	3	3
5	5	5	5	5
6	6	6	6	6
7	7	8	8	8
8	8	7	7	7
9	9	9	9	9
10	10	11	11	12
11	11	10	10	10
12	12	12	12	11
13	13	13	14	15
14	14	14	13	13
15	15	17	17	17
16	16	15	15	14
17	17	16	16	16
18	18	18	18	18
19	19	–99	–99	–99
20	20	19	20	20
21	21	21	23	23
22	22	20	19	19
23	23	23	21	21
24	24	22	22	22
25	25	24	24	25
26	26	24	25	24
27	27	25	26	26
28	28	27	28	27
29	29	26	27	26
30	30	28	29	28

Sequential index	Tracking index (four-frame sequence)			
31	31	29	30	29
32	32	30	31	32
33	33	32	35	34
34	34	37	38	37
35	35	34	36	36
36	35	36	33	30
37	36	33	39	39
38	37	31	32	31
39	38	35	37	35
40	39	38	34	33
41	40	40	41	43
42	41	44	45	47
43	42	39	40	38
44	43	41	41	42
45	44	43	43	41
46	45	45	44	44
47	46	42	43	40
48	47	46	46	45
49	48	47	47	46
50	49	48	48	48
51	50	49	49	49
52	51	50	50	50
53	52	52	52	52
54	53	51	51	51
55	54	53	53	53
56	55	54	54	54
57	56	55	55	56
58	57	56	56	55
59	58	58	58	58
60	59	57	57	57

Sequential index	Tracking index (four-frame sequence)			
61	60	59	59	60
62	61	60	60	62
63	62	61	61	61
64	63	62	62	63
65	64	64	64	67
66	65	65	63	64
67	66	63	65	66
68	67	66	66	65
69	68	67	67	68
70	69	68	68	68
71	70	69	69	70
72	71	70	70	72
73	72	71	71	69
74	73	73	72	74
75	74	72	70	72
76	75	75	74	76
77	76	74	73	75
78	77	77	75	78
79	78	78	77	77
80	79	76	78	79
81	80	79	76	73
82	81	80	79	80
83	82	81	80	81
84	83	82	81	82
85	84	83	82	83
86	85	–99	–99	–99
87	86	–99	–99	–99

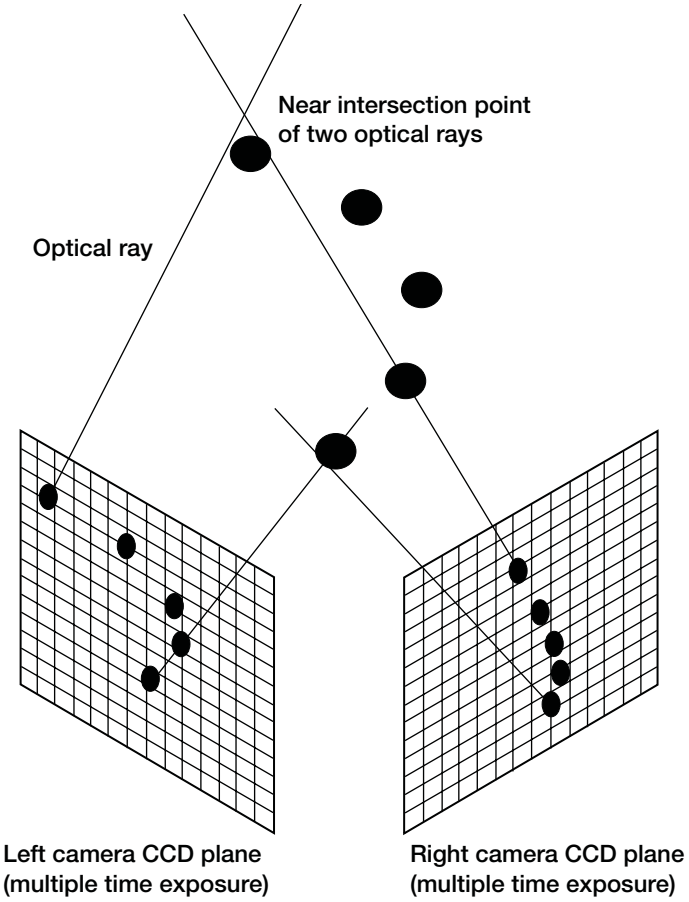

Figure 9.—Stereo matching of a track that appears in the right and left orthogonal camera views. CCD, charge-coupled device camera.

a given track from the left view with one in the right view. This is similar to the approach taken by Guezennec et al. (1994). A threshold value was chosen for the sum of the squared errors. Any pair of tracks having an error exceeding this value was rejected. Table VII lists the stereo-matching data file when stereo matching the left and right images. The output from the stereo-matching technique can be used as a measure of how successful the tracking algorithm may have been since, ideally, tracks identified in one view should each match exactly with a unique track in the orthogonal view.

TABLE VII.—STEREO-MATCHING DATA FILE FOR LEFT AND RIGHT PARTICLE TRACKING DATA

[The index is listed first, then the four-frame sequence with the top row representing the left view and the bottom row representing the right view.]

Sequential index	Tracking index (four-frame sequence)			
0	0	0	0	0
	0	0	0	0
1	1	1	1	1
	1	1	1	1
2	2	3	4	4
	2	4	4	4
3	3	2	2	2
	3	2	2	2
4	4	4	3	3
	4	3	3	3
5	5	5	5	5
	5	5	5	5
6	6	6	6	6
	6	6	6	6
7	7	7	7	8
	7	8	8	8
8	8	8	8	7
	8	7	7	7
9	9	9	9	9
	9	9	9	9
10	10	10	11	12
	10	11	11	12
11	11	11	10	10
	11	10	10	10
12	12	12	12	11
	12	12	12	11
13	13	13	13	15
	13	13	14	15
14	14	14	14	13
	14	14	13	13
15	15	15	17	17
	15	17	17	17
16	16	16	15	14
	16	15	15	14
17	17	17	16	16
	17	16	16	16
18	18	18	18	18
	18	18	18	18
19	19	19	19	20
	20	19	20	20
20	20	22	22	24
	21	21	23	23
21	21	21	20	19
	22	20	19	19
22	22	20	21	21
	23	23	21	21
23	23	23	23	22
	24	22	22	22
24	24	24	24	23
	26	24	25	24
25	25	25	25	25
	25	24	24	25
26	27	26	26	26
	27	25	26	26
27	28	27	27	27
	29	26	27	26
28	29	29	28	28
	28	27	28	27
29	30	28	29	29
	30	28	29	28
30	31	30	30	30
	31	29	30	29
31	32	31	31	35
	32	30	31	32
32	33	32	33	36
	33	32	35	34
33	34	33	35	32
	37	31	32	31
34	35	39	38	41
	36	33	39	39
35	36	34	32	33
	38	35	37	35
36	37	38	36	37
	35	34	36	36
37	38	36	37	38
	34	37	38	37
38	39	35	34	31
	35	36	33	30
39	40	37	32	34
	39	38	34	33
40	42	42	40	40
	40	40	41	43
41	43	41	39	39
	42	39	40	38
42	44	43	43	44
	46	42	43	40
43	45	45	45	47
	41	44	45	47
44	46	44	42	43
	44	43	43	41
45	47	48	47	49
	48	47	47	46
46	48	46	44	45
	45	45	44	44
47	49	47	46	46
	47	46	46	45
48	50	49	48	48
	49	48	48	48
49	51	51	49	51
	50	49	49	49
50	52	50	50	50
	51	50	50	50
51	53	53	51	52
	53	51	51	51
52	54	54	52	54
	52	52	52	52
53	55	55	52	53
	54	53	53	53
54	56	56	53	55
	55	54	54	54
55	57	57	54	56
	56	55	55	56
56	58	58	55	57
	57	56	56	55
57	59	60	57	59
	60	59	59	60
58	60	59	56	58
	58	58	58	58
59	62	63	59	61
	61	60	60	62
60	63	64	60	63
	64	64	64	67

TABLE VII (continued).—STEREO-MATCHING DATA FILE FOR LEFT AND RIGHT PARTICLE TRACKING DATA

Sequential index	Tracking index (four-frame sequence)			
61	64	62	61	63
	63	62	62	63
62	65	66	62	64
	67	66	66	65
63	66	67	63	65
	66	63	65	66
64	67	68	66	68
	67	66	66	65
65	68	69	64	66
	68	67	67	68
66	69	65	67	62
	67	66	66	65
67	70	70	65	67
	69	68	68	68
68	71	71	68	69
	72	71	71	69
69	72	73	71	70
	71	70	70	72
70	73	74	70	72
	74	72	70	72

Sequential index	Tracking index (four-frame sequence)			
71	74	75	72	73
	73	73	72	74
72	75	77	73	77
	77	77	75	78
73	76	72	69	71
	70	69	69	70
74	77	77	74	77
	79	76	78	79
75	79	80	78	80
	79	76	78	79
76	80	78	76	76
	78	78	77	77
77	81	79	75	75
	80	79	76	73
78	82	81	79	81
	81	80	79	80
79	83	82	77	78
	81	80	79	80
80	84	83	77	78
	82	81	80	81

Sequential index	Tracking index (four-frame sequence)			
81	85	84	80	79
	81	80	79	80

Summary of Results

A new three-dimensional (3D), full-field analysis technique has been developed for industrial and space applications. Stereo imaging velocimetry (SIV) will permit the collection of quantitative, 3D flow data from any optically transparent fluid that can be seeded with tracer particles. The goal of SIV is to provide a means to measure 3D fluid velocities quantitatively and qualitatively at many points. SIV is applicable to any system with an optically transparent fluid seeded with tracer particles. Except for the tracer particles, this measurement technique is nonintrusive. Velocity accuracies are on the order of 95 to 99 percent of full-field. The system components of SIV include 3D camera calibration, particle overlap decomposition, particle tracking, and stereo matching. SIV has been used successfully for space shuttle experiments as well as in fluid flow applications for business and industry.

Glenn Research Center
National Aeronautics and Space Administration
Cleveland, Ohio, May 5, 2004

Appendix—Symbols

A_i, B_i, C_i, D_i	calibration coefficients
assigned_particle_usage [f, j]	the number of times particle j in frame f appears within any track from a particular assignment of tracks
b, c, q, t	parameter values
C_R	camera-dependent constant with units of millimeters per pixel
D	distance between a camera and the face of the chamber
d	horizontal distance of a camera axis from the origin
est	estimated position of a particle
F	number of frames in a track
f	focal length of a camera
$f( )$	penalty function defined as a mapping from the parameters shown, with $-2.0 < f( ) < 2.0$
id	track identification number
max$R$, min$R$	maximum and minimum track search radius
N_f	number of particles in a frame f, $1 \le f \le F = 4$
N_1	number of tracks (the number of particles in frame 1)
$P( )$	probability of an object consisting of one, two, or three particles
particle_usage_error	$\sum_{f=1}^{F} \sum_{j=1}^{N_f} \lvert \text{assigned\_particle\_usage}[f, j] - 1 \rvert$
track_error	$\sum_{j=1}^{N_1} f$ (track_straightness_error[j], track_smoothness_error[j])
usageCoeff	weighting of the usage relative to the track error
$X_R^i Z_R^i \left(Y_L^i \; Z_L^i \right)$	window coordinates of particle on the right (left) face of the chamber
x	value of the feature
$x_i \, y_i \, z_i$	absolute $x \, y \, z$ coordinates of particle i
$x_R^i z_R^i \left(y_L^i \; z_L^i \right)$	pixel coordinates of particle i as seen by the right (left) camera
Δ	vertical distance of a camera axis from the origin
Δ_3, Δ_4	difference between the actual and estimated position (based on an assumption of zero acceleration) for particles 3 and 4

Subscripts

L	left camera
R	right camera

References

Bethea, Mark D. (1996): High Precision Algorithms for Stereo Imaging Velocimetry. Ph.D. Thesis, Case Western Reserve University.

Bethea, M.D.; Lock, J.A.; and Merat F. (1997): Three-Dimensional Camera Calibration Technique for Stereo Imaging Velocimetry Experiments. Opt. Eng., vol. 36, no. 12, pp. 3445–3454.

Crouser, Paul D.; Bethea, Mark D.; and Merat, Frank L. (1995): An Evolutionary, Neural Net Model for Globally-Optimized Particle Tracking. Paper presented at the Ohio Aerospace Institute Neural Network Symposium and Workshop 95, Brook Park, Ohio.

Guezennec, Y.G.; and Kiritsis, N. (1990): Statistical Investigation of Errors in Particle Image Velocimetry. Exp. Fluids, vol. 10, no. 2–3, pp. 138–146.

Guezennec, Y.G., et al. (1994): Algorithms for Fully Automated Three-Dimensional Particle Tracking Velocimetry. Exp. Fluids, vol. 17, no. 4, pp. 209–210.

Haralick, Robert M.; and Shapiro, Linda G. (1992): Computer and Robot Vision. Addison-Wesley, Reading, MA.

McDowell, Mark; and Glasgow, Thomas K. (1999): Stereo Imaging Velocimetry. U.S. Patent 5,905,568, May.

Miller, B.B.; Meyer, M.B.; and Bethea, M.D. (1994): Stereo Imaging Velocimetry for Microgravity Applications. Proc. Soc. Photo Opt. Instrum. Eng., vol. 2210, pp. 260–270.

Pao, Yoh-Han (1989): Adaptive Pattern Recognition and Neural Networks. Addison-Wesley, Reading, MA.

REPORT DOCUMENTATION PAGE

Form Approved
OMB No. 0704-0188

1. AGENCY USE ONLY (*Leave blank*)	2. REPORT DATE	3. REPORT TYPE AND DATES COVERED
	December 2004	Technical Paper

4. TITLE AND SUBTITLE

Stereo Imaging Velocimetry Technique Using Standard Off-the-Shelf CCD Cameras

5. FUNDING NUMBERS

WBS–22–400–35–80–01

6. AUTHOR(S)

Mark McDowell and Elizabeth Gray

7. PERFORMING ORGANIZATION NAME(S) AND ADDRESS(ES)

National Aeronautics and Space Administration
John H. Glenn Research Center at Lewis Field
Cleveland, Ohio 44135–3191

8. PERFORMING ORGANIZATION REPORT NUMBER

E–14586

9. SPONSORING/MONITORING AGENCY NAME(S) AND ADDRESS(ES)

National Aeronautics and Space Administration
Washington, DC 20546–0001

10. SPONSORING/MONITORING AGENCY REPORT NUMBER

NASA TP—2004-213112

11. SUPPLEMENTARY NOTES

Mark McDowell, NASA Glenn Research Center; and Elizabeth Gray, Scientific Consulting, Inc., 17418 Puritas Avenue, Cleveland, Ohio 44135. Responsible person, Mark McDowell, organization code 6728, 216–433–8161.

12a. DISTRIBUTION/AVAILABILITY STATEMENT

Unclassified - Unlimited
Subject Category: 70 Distribution: Nonstandard

Available electronically at http://gltrs.grc.nasa.gov

This publication is available from the NASA Center for AeroSpace Information, 301–621–0390.

12b. DISTRIBUTION CODE

13. ABSTRACT ***(Maximum 200 words)***

Stereo imaging velocimetry is a fluid physics technique for measuring three-dimensional (3D) velocities at a plurality of points. This technique provides full-field 3D analysis of any optically clear fluid or gas experiment seeded with tracer particles. Unlike current 3D particle imaging velocimetry systems that rely primarily on laser-based systems, stereo imaging velocimetry uses standard off-the-shelf charge-coupled device (CCD) cameras to provide accurate and reproducible 3D velocity profiles for experiments that require 3D analysis. Using two cameras aligned orthogonally, we present a closed mathematical solution resulting in an accurate 3D approximation of the observation volume. The stereo imaging velocimetry technique is divided into four phases: 3D camera calibration, particle overlap decomposition, particle tracking, and stereo matching. Each phase is explained in detail. In addition to being utilized for space shuttle experiments, stereo imaging velocimetry has been applied to the fields of fluid physics, bioscience, and colloidal microscopy.

14. SUBJECT TERMS	15. NUMBER OF PAGES
Fluid flow; Fluidics	24
	16. PRICE CODE

17. SECURITY CLASSIFICATION OF REPORT	18. SECURITY CLASSIFICATION OF THIS PAGE	19. SECURITY CLASSIFICATION OF ABSTRACT	20. LIMITATION OF ABSTRACT
Unclassified	Unclassified	Unclassified	